

# Application of a momentum-space semi-locally regularized chiral potential to selected disintegration processes

V. Urbanevych , R. Skibiński , H. Witała , J. Golak, K. Topolnicki, and A. Grassi  
*M. Smoluchowski Institute of Physics, Jagiellonian University, PL-30348 Kraków, Poland*

E. Epelbaum and H. Krebs

*Ruhr-Universität Bochum, Fakultät für Physik und Astronomie, Institut für Theoretische Physik II, D-44780 Bochum, Germany*



(Received 31 July 2020; accepted 19 January 2021; published 11 February 2021)

We apply a recently developed momentum-space semilocally regularized chiral potential to the  $^2\text{H}$  and  $^3\text{He}$  photodisintegration processes and to the (anti)neutrino induced deuteron breakup reactions. Specifically, the differential cross section, the photon analyzing power, and the final proton polarization have been calculated for deuteron photodisintegration at photon energies of 30 and 100 MeV. For  $^3\text{He}$  photodisintegration, predictions for the semi-inclusive and exclusive differential cross sections are presented for photon energies up to 120 MeV. The total cross section is calculated for (anti)neutrino disintegration of the deuteron for (anti)neutrino energies below 200 MeV. Predictions based on the Argonne V18 potential and on an older chiral force with regularization applied in coordinate space are used for comparison. Using the fifth-order chiral nucleon-nucleon potential supplemented with dominant contributions from the sixth order allows us to obtain converged predictions for observables in the investigated reactions. Our results based on the newest semilocal chiral potentials show even smaller cutoff dependence and a somewhat faster convergence for the considered electroweak observables than the previously reported ones with a coordinate-space regulator, which make them a promising tool to study electroweak processes.

DOI: [10.1103/PhysRevC.103.024003](https://doi.org/10.1103/PhysRevC.103.024003)

## I. INTRODUCTION

Chiral effective field theory ( $\chi\text{EFT}$ ) is nowadays the most reliable approach to study low-energy nuclear forces. Its continuous development for nearly 30 years resulted in advanced two-nucleon (2N) and many-nucleon interactions [1–10].

In 2018 the Bochum group presented a new version of the chiral interaction [1], which differs from their previous realization [5,11], among others, by the regularization scheme applied directly in momentum space. This semilocal momentum-space (SMS) regularized potential has been derived completely up to the fifth order ( $\text{N}^4\text{LO}$ ) of the chiral expansion and even some contributions from the sixth order have been included in its “ $\text{N}^4\text{LO}^+$ ” version. Up to now this potential has been used out of necessity in the 2N system to fix its free parameters and later applied to nucleon-deuteron elastic scattering as well as to the nucleon induced deuteron breakup process [12,13], delivering at  $\text{N}^2\text{LO}$  a data description of a similar quality as nonchiral semiphenomenological potentials. In this paper we extend applications of this SMS interaction beyond the purely strong processes to a few electroweak reactions.

Investigations of the electroweak processes with older chiral forces with nonlocal regularization resulted in predictions strongly dependent on the cutoff parameter (see, e.g., [14–16]). Such a picture was observed with the single-nucleon current and with inclusion of some meson-exchange

currents. In 2016 we showed [17] that with a semilocal coordinate-space regularized chiral potential (SCS) [5,11] one can reduce such big variations with respect to the regulator, but predictions were still clearly dependent on the cutoff parameter. In the present paper we check if properties of the SMS potential match or possibly even surpass those of the former version of the chiral potential. To this end we apply the SMS chiral potential to selected electromagnetic and weak processes. Specifically we study the  $\gamma + ^2\text{H} \rightarrow p + n$ ,  $\nu_e + ^2\text{H} \rightarrow \nu_e + p + n$ ,  $\bar{\nu}_e + ^2\text{H} \rightarrow \bar{\nu}_e + p + n$ ,  $\bar{\nu}_e + ^2\text{H} \rightarrow e^+ + n + n$ , and  $\gamma + ^3\text{He} \rightarrow p + p + n$  reactions. For the sake of comparison we also use the results of our previous research with the SCS [5,11] and with the Argonne V18 (AV18) potential [18].

One of the most challenging problems with the application of a nucleon-nucleon (NN) potential to electroweak processes with nuclear systems is the construction of consistent 2N and, more generally, many-nucleon electroweak current operators [19]. Many-nucleon currents linked to various models of nuclear forces have been investigated for a long time (see, e.g., [20–26]). No full 2N electromagnetic or weak current operator consistent with the SMS chiral force has been derived yet (see, however, [27] for a recent calculation of the deuteron structure radius with a consistent 2N charge operator). Thus we rely on the single-nucleon current (SNC) and use the Siegert theorem to take into account many-body contributions to the nuclear electromagnetic current. Many-nucleon currents, even

included implicitly, are absolutely indispensable in a correct treatment of photonuclear reactions. It has been shown (see, for example, [28]) that their omission leads to incorrect predictions, especially for polarization observables. In the case of weak reactions we use the nonrelativistic form of the single-nucleon weak current operator, the components of which are defined in Ref. [29]. The dominant role of the single-nucleon weak current in neutrino scattering of the deuteron has been recently demonstrated by Baroni and Schiavilla [26], who have found only a few-percent contribution from higher-order current operators.

The rest of this paper is structured as follows. In the next section we briefly describe our formalism and then in Sec. III we show our results for the deuteron photodisintegration and (anti)neutrino induced deuteron disintegration processes. Section IV comprises our predictions for  $^3\text{He}$  disintegration. We summarize and conclude in Sec. V.

## II. THEORETICAL FORMALISM

Our approach, which is based on the Schrödinger and Lippmann-Schwinger equations (for 2N reactions) and on the Faddeev formalism [for three-nucleon (3N) reactions], has been described in detail in Refs. [28–30]. In short, the path to the observables for the electromagnetic or weak disintegrations leads through the appropriate nuclear matrix elements.

For the deuteron photodisintegration process, in the nuclear matrix elements

$$N_{\text{deu}}^\mu \equiv \langle \Psi_{\text{scatt}}^{2N} | j_{2N}^\mu | \Psi_{\text{bound}}^{2N} \rangle, \quad (2.1)$$

a full 2N electromagnetic current operator appears between the initial deuteron bound state  $|\Psi_{\text{bound}}^{2N}\rangle$  and the final 2N scattering state  $|\Psi_{\text{scatt}}^{2N}\rangle$ . In order to obtain the deuteron bound state we solve the Schrödinger equation with a given 2N potential  $V$ . Further, the scattering state is constructed from a solution of the Lippmann-Schwinger equation for the  $t$  operator:  $t = V + tG_0V$ , where  $G_0$  is a free 2N propagator. Using this equation, (2.1) takes the form

$$N_{\text{deu}}^\mu = \langle \vec{p}_0 | (1 + tG_0) j_{2N}^\mu | \Psi_{\text{bound}}^{2N} \rangle, \quad (2.2)$$

where  $|\vec{p}_0\rangle$  is the antisymmetrized eigenstate of the relative proton-neutron momentum.

Our formalism for the (anti)neutrino induced deuteron disintegrations is essentially the same [29,31,32]. Especially, for the neutral-current (NC) driven processes the isospin structure of the current operator and the 2N final state are the same as for the photodisintegration reaction. In the case of the charged-current (CC) driven reaction only some straightforward modifications are introduced in the corresponding weak single-nucleon current operator.

For the  $^3\text{He}$  photodisintegration with three free nucleons in the final state, if the 3N force is neglected, the nuclear matrix elements are given as [28]

$$N_{3N}^\mu = \langle \Phi_{3N} | (1 + P) j_{3N}^\mu | \Psi_{\text{bound}}^{3N} \rangle + \langle \Phi_{3N} | (1 + P) | U^\mu \rangle, \quad (2.3)$$

where  $|\Psi_{\text{bound}}^{3N}\rangle$  represents the initial 3N bound state and  $|\Phi_{3N}\rangle$  is an antisymmetrized state which describes the free motion of three outgoing nucleons. Further, the permutation operator

$P$  is built from transpositions  $P_{ij}$  of particles  $i$  and  $j$ :  $P = P_{12}P_{23} + P_{13}P_{23}$  and the auxiliary state  $|U^\mu\rangle$  allows us to include all the final-state interactions among the three outgoing nucleons. It is a solution of the Faddeev-like equation [28], which reads

$$|U^\mu\rangle = t\tilde{G}_0(1 + P)j_{3N}^\mu|\Psi_{\text{bound}}^{3N}\rangle + t\tilde{G}_0P|U^\mu\rangle, \quad (2.4)$$

where  $\tilde{G}_0$  is a free 3N propagator and  $j_{3N}^\mu$  is the total 3N electromagnetic current operator.

At the moment, 2N currents, with the same regularization as used in the SMS interaction investigated here, are not available. While their operator form has been already derived [25,33–37], a consistent regularization of these currents is still under development. Thus for the weak processes we use contributions from the single-nucleon currents only. In the case of the electromagnetic reactions additional contributions are taken implicitly into account using the Siegert theorem, as described in detail in Refs. [16,28,30]. We partly substitute electric multipoles by the Coulomb ones, calculated from the single-nucleon charge density operator. To this end we carry out the multipole decomposition of the corresponding SNC matrix elements.

It should be stressed that a complete treatment of the considered reactions in  $\chi\text{EFT}$  will require an application of consistent three-nucleon forces (in systems with more than two nucleons) and currents fulfilling the continuity equation (see [19] for details and for a discussion of challenges that need to be tackled). That ambitious aim is not unrealistic but requires in the first step reliable nuclear forces which reproduce nuclear structure and three-body continuum phenomenology. Using the SMS regularization such interactions are being constructed up to  $N^4\text{LO}$  order of chiral expansion by the LENPIC Collaboration [38].

We perform our calculations in momentum space, in the partial wave decomposition scheme. For the deuteron disintegration we take into account all partial waves in the 2N system up to the total angular momentum  $j = 4$ . For  $^3\text{He}$  photodisintegrations we use all two-nucleon partial waves up to the total 2N angular momentum  $j = 3$  and all three-nucleon partial waves up to the total 3N angular momentum  $J = \frac{15}{2}$ . For further details on our computational scheme see [28].

## III. RESULTS FOR $^2\text{H}$ DISINTEGRATION

First we discuss our results for the deuteron photodisintegration process  $\gamma + ^2\text{H} \rightarrow p + n$  at two laboratory photon energies  $E_\gamma = 30$  and 100 MeV. Figure 1 shows the differential cross section  $\frac{d^2\sigma}{d\Omega}$  obtained using the chiral SMS potential for both energies. For the sake of comparison we also show predictions obtained using the AV18 NN potential [18]. Both for the chiral SMS force and for the AV18 potential our predictions were obtained with the single-nucleon current supplemented implicitly by some 2N parts, using the Siegert theorem [14].

In the left column of Fig. 1 we present results calculated at different chiral orders (from LO to  $N^4\text{LO}^+$ ) with the regularization parameter  $\Lambda = 450$  MeV. For the energy  $E_\gamma = 30$  MeV (top row) only the LO prediction is noticeably separated from all others and the difference among remaining

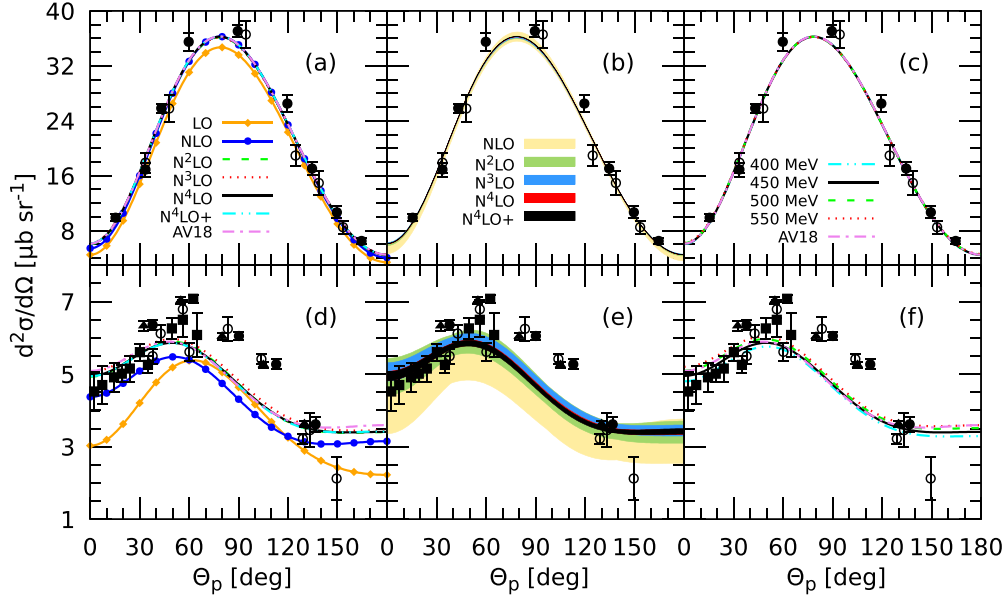


FIG. 1. The differential cross section  $\frac{d^2\sigma}{d\Omega}$  for the  $\gamma + {}^2\text{H} \rightarrow p + n$  reaction at the laboratory photon energy  $E_\gamma = 30$  MeV (top) and  $E_\gamma = 100$  MeV (bottom) as a function of the proton emission angle  $\theta_p$  (the angle between the initial photon momentum and the proton momentum) in the center-of-mass frame. The left column shows the dependence of predictions on the order of chiral expansion. The orange solid line with diamonds, the blue solid line with circles, and the green dashed, the red dotted, the black solid, the cyan double-dot-dashed, and the violet dot-dashed curves correspond to the LO, NLO,  $\text{N}^2\text{LO}$ ,  $\text{N}^3\text{LO}$ ,  $\text{N}^4\text{LO}$ ,  $\text{N}^4\text{LO}+$ , and AV18 potential based predictions, respectively. Truncation errors for the different orders of chiral expansion are presented in the middle column. The yellow band shows the truncation errors at NLO, the green band shows the truncation errors at  $\text{N}^2\text{LO}$ , the blue band shows the truncation errors at  $\text{N}^3\text{LO}$ , the red band shows the truncation errors at  $\text{N}^4\text{LO}$ , and finally the black band shows the truncation errors at  $\text{N}^4\text{LO}+$  order. The right column shows the chiral SMS predictions at  $\text{N}^4\text{LO}$ , calculated using different values of the cutoff parameter  $\Lambda$ . The cyan double-dot-dashed, the black solid, the green dashed, the red dotted, and the violet dot-dashed curves correspond to  $\Lambda = 400, 450, 500,$  and  $550$  MeV and the AV18 based predictions, respectively. For the predictions shown in the left and in the middle columns the regulator value  $\Lambda = 450$  MeV is used. The data points at 30 MeV are the same as in Ref. [42] and those at 100 MeV are taken from [42] (open and filled circles, squares) and from [43] (triangles).

predictions is very small:  $\approx 0.06\%$  at the maximum of the cross section between  $\text{N}^2\text{LO}$  and  $\text{N}^3\text{LO}$  results and even less for all subsequent chiral orders. This shows that for this photon energy the SMS potential based predictions converge rapidly and contributions from high orders are not crucial. At 100 MeV our predictions converge more slowly, but starting from  $\text{N}^2\text{LO}$  all the curves are very close to each other (the difference between the lines remains below 3%). In the case of  $E_\gamma = 100$  MeV the data description is worse than at  $E_\gamma = 30$  MeV, but based on the semiphenomenological results by Arenhövel and Sanzone [39] it is expected that for higher energies 2N electromagnetic currents contribute substantially and we thus expect that our predictions will improve significantly when explicit 2N current operators, fully consistent with the 2N potential, are included.

The middle column of Fig. 1 presents the truncation errors arising, at a given chiral order, due to neglecting of higher-order contributions to the considered observables. These theoretical estimates were calculated employing the prescription advocated in Ref. [40] and later used also for electromagnetic reactions with the SCS potential in Ref. [17].<sup>1</sup>

<sup>1</sup>It is also possible to perform a more sophisticated estimation based on the Bayesian approach [12,41]; however, for the sake of comparison with [17] we use the prescription from [40] in this paper.

The observed picture demonstrates that only tiny contributions from the potential components above  $\text{N}^4\text{LO}+$  should be expected, as the band showing the truncation error for the highest presented chiral order  $\text{N}^4\text{LO}+$  is quite narrow—its width in the maximum of the cross section is around 0.07% (2.7%) of the cross-section magnitude at the photon energy  $E_\gamma = 30$  MeV (100 MeV). Notice, however, that the estimates of truncation error may change upon performing a more complete treatment of the current operators.

Finally, the right column of Fig. 1 shows the dependence of our predictions on the value of the regularization parameter  $\Lambda$  in the range  $\Lambda \in [400, 550]$  MeV. It is clearly seen that the SMS potential provides us with a weak dependence of the predicted cross section on the cutoff parameter at both investigated energies. This is an important improvement compared to older versions of chiral forces, such as the SCS chiral potential [17], where regularization strongly influenced the results, yielding a spread of predictions up to 20% for small proton scattering angles at  $E_\gamma = 100$  MeV.

Our previous investigations [17] were devoted to the application of the older version of the NN potential, namely, the chiral SCS force, to selected electroweak processes. In particular, this potential applied to the deuteron photodisintegration reaction yields predictions for the differential cross section well converged with respect to the order of chiral expansion. Now we are in a position to compare the outcomes

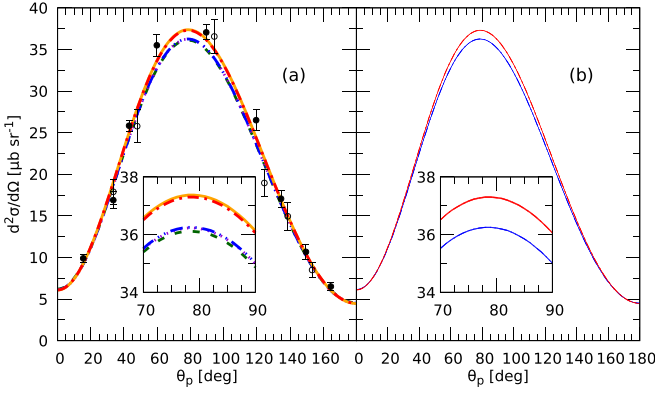


FIG. 2. The differential cross section  $\frac{d^2\sigma}{d\Omega}$  at  $E_\gamma = 30$  MeV as a function of the proton emission angle  $\theta_p$  calculated using the SCS (with  $R = 0.9$  fm) and the SMS (with  $\Lambda = 450$  MeV) chiral potentials. (a) Predictions at higher orders of chiral expansion [ $N^3$ LO,  $N^4$ LO, and  $N^4$ LO+ (for the SMS force only)]. The dashed green, dotted violet, and double-dot-dashed blue lines represent results calculated using the SMS potential up to  $N^3$ LO,  $N^4$ LO, and  $N^4$ LO+, respectively. The solid orange and the dash-dotted red lines are obtained using the SCS potential at  $N^3$ LO and  $N^4$ LO, respectively. All data points (open and filled circles) are taken from [42]. (b) SCS (SMS) potential based result at  $N^4$ LO ( $N^4$ LO+) given by the dash-dotted red (double-dash dotted blue) curve and corresponding truncation error represented by the pink (blue) band. Both for the SCS and the SMS forces, predictions and bands overlap.

from the SMS and from the SCS potentials. Results of our calculations of the differential cross section obtained using higher chiral orders (starting from  $N^3$ LO) of these two forces are presented in Figs. 2 and 3 for the photon energy 30 and 100 MeV, respectively. It is interesting that, despite the convergence of both potentials, curves approach different values of the cross section and quite a big gap between predictions of the SMS and SCS potentials is visible in both figures including the inset in Fig. 2. The difference between the  $N^4$ LO SMS and SCS cross sections at  $E_\gamma = 30$  MeV reaches  $1.07 \mu\text{b sr}^{-1}$  ( $\approx 3\%$ ) at  $\theta_p = 79^\circ$  and  $0.467 \mu\text{b sr}^{-1}$  ( $\approx 8\%$ ) at  $\theta_p = 52^\circ$  for  $E_\gamma = 100$  MeV. The observed deviation can be

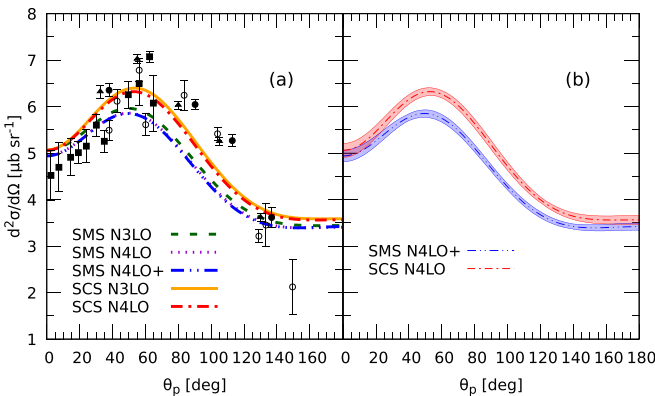


FIG. 3. The same as in Fig. 2 but for  $E_\gamma = 100$  MeV. For the description of curves and bands see Fig. 2. Data are taken from [43] (triangles) and from [42] (open and filled circles and squares).

caused by the fact that the potentials use different values of low-energy constants, which results also in different deuteron wave functions. It is also possible that the lack of explicit 2N current contributions affects differently the predictions based on the two potentials. Absence of such gaps for full calculations, that is, calculations including electromagnetic 2N current operators that are complete and consistent with the NN interaction, will be a challenging test for the chiral approach. In addition, in Figs. 2(b) and 3(b) we compare predictions of the SMS and SCS forces at the highest available orders, i.e.,  $N^4$ LO+ and  $N^4$ LO, showing also their uncertainties arising from truncation errors computed within the method of [40]. At both energies the difference between predictions surpasses magnitudes of their uncertainties, which should not come as a surprise given that our calculations are incomplete. In the case of the cross section at  $E_\gamma = 30$  MeV the bands representing truncation errors are so narrow that they overlap with curves illustrating our predictions.

It is also worth mentioning that one has to be cautious about judging the agreement between predictions obtained with the two potentials as, besides the various regularization schemes, they differ in other aspects [1]. An important difference between the SMS and SCS potentials is the removal of the redundant contact interactions at the order  $N^3$ LO which makes them softer. Another difference is that the values of the pion-nucleon low-energy constants determined from matching chiral perturbation theory to the Roy-Steiner-equation analysis of pion-nucleon scattering [44] are used in the SMS force. Last but not least, the SMS interaction has been fitted to NN scattering data while the SCS one has been fitted to the results of the Nijmegen partial wave analysis [45]. Even regarding the regularization method itself it is not possible to establish a one-to-one correspondence between particular values of regulators in the two schemes. The prescription given in Ref. [46],  $\frac{2}{R} \leftrightarrow \Lambda$ , yields  $\Lambda \approx 438$  MeV for  $R = 0.9$  fm. This means that  $\Lambda = 450$  MeV and  $R = 0.9$  fm deliver only approximately the same regularization effect.

Nevertheless, since for the SMS potential its version for  $\Lambda = 450$  MeV is available, here and in other cases where results based on the two potentials are compared, we use the accessible pair of regulators:  $R = 0.9$  fm and  $\Lambda = 450$  MeV. For the calculations presented here the comparison with experimental data cannot be used to judge between both forces because depending on the photon energy or the proton scattering angle either one or the other prediction is closer to the data. Moreover, the inclusion of consistent two-body currents may change predictions differently for both interactions.

In Figs. 4 and 5 we compare predictions based on the two chiral potentials, SMS and SCS, more closely. We show the relative difference between the differential cross section for all the presented chiral orders. To this end, we define  $\delta\sigma(\text{chiral order})$  as a difference between the maximum and minimum values of  $\frac{d^2\sigma}{d\Omega}$  among predictions at orders from LO to  $N^4$ LO ( $N^4$ LO+) for the SCS (SMS) forces for each angle  $\theta_p$  and divide it by the mean value from five (six) predictions for the SCS (SMS), correspondingly. The resulting quantity both for the SMS (solid green line) and for the SCS (dashed violet line) potentials is presented as a function of the proton detection angle in Fig. 4(a) for  $E_\gamma = 30$  MeV, and Fig. 5(a)



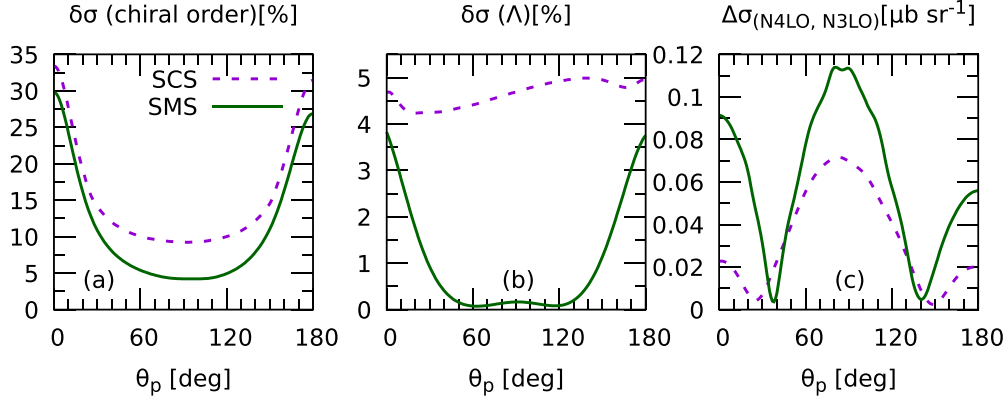


FIG. 4. The relative spread of predictions for the differential cross section for the deuteron photodisintegration reaction at the initial photon energy  $E_\gamma = 30$  MeV. (a) Difference between maximum and minimum values of the differential cross section for all chiral orders used, divided by its average (from LO to  $N^4\text{LO}^+$  for the SMS potential, green solid line; from LO to  $N^4\text{LO}$  for the SCS, violet dashed line). (b) Analogous quantity, but measuring the spread with respect to the different cutoff values used (from 400 to 550 MeV for the SMS force and from 0.8 to 1.2 fm for the SCS potential) at fixed chiral order ( $N^4\text{LO}$ ). (c) Absolute difference between  $\frac{d^2\sigma}{d\Omega}$  calculated at  $N^4\text{LO}$  and  $N^3\text{LO}$  for each of two potentials.

for  $E_\gamma = 100$  MeV. In both cases  $\delta\sigma(\text{chiral order})$  is larger with the SCS potentials than with the SMS potentials, which means that the net spread with respect to chiral orders with the SMS potentials is smaller than with the SCS potentials. Nevertheless this observation can also be an effect of the leading-order predictions, which for the SMS as well as for the SCS case are far away from all the other results. Therefore it is interesting to check the absolute difference between differential cross sections at  $N^3\text{LO}$  and  $N^4\text{LO}$  for the two potentials, which is done in Figs. 4(c) and 5(c). One can see that for both energies the difference between  $N^3\text{LO}$  and  $N^4\text{LO}$  is larger with the SMS potential than with the SCS potential for nearly all scattering angles. Thus the contribution from corrections at  $N^4\text{LO}$  is actually larger with the SMS potentials than with the SCS potentials.

Figures 4(b) and 5(b) show  $\delta\sigma(\Lambda)$ , which is an analogous quantity to what is shown in Figs. 4(a) and 5(a), but now defined with respect to the values of the regularization parameter. That means that  $\delta\sigma(\Lambda)$  is the difference between the largest and the smallest value of  $\frac{d^2\sigma}{d\Omega}$ , calculated using all values of the cutoff parameter ( $R$  for the SCS and  $\Lambda$  for the

SMS) divided by its average  $\sigma_{\text{avg}}(\Lambda)$ . From the figure it is clear that dependence on the cutoff parameter is much weaker for the SMS potential. Note, however, that this spread depends of course strongly on the range used for the regularization parameter. In particular, for the SCS interaction this includes softer regulators up to  $R = 1.2$  fm, which may introduce artifacts in the potential, leading to a wider spread of the predictions.

Figure 6 demonstrates convergence of the cross section with respect to the chiral order. Each of the panels represents a certain combination of the photon energy and the proton emission angle:  $E_\gamma = 30$  MeV,  $\theta_p = 60^\circ$  in Fig. 6(a);  $E_\gamma = 100$  MeV,  $\theta_p = 15^\circ$  in Fig. 6(b); and  $E_\gamma = 100$  MeV,  $\theta_p = 150^\circ$  in Fig. 6(c). The quantity presented in this figure is the absolute difference between differential cross section  $\frac{d^2\sigma}{d\Omega}$  at each of two subsequent orders: the order given by the corresponding value on the  $x$  axis and the subsequent order. For example, the value with  $x$  coordinate NLO is nothing but  $|\frac{d^2\sigma}{d\Omega}|_{N^2\text{LO}} - \frac{d^2\sigma}{d\Omega}|_{\text{NLO}}|$ . We see that the SCS potential tends to converge faster, at least at presented scattering angles, since the difference shown in Fig. 6 drops to zero earlier. This is in

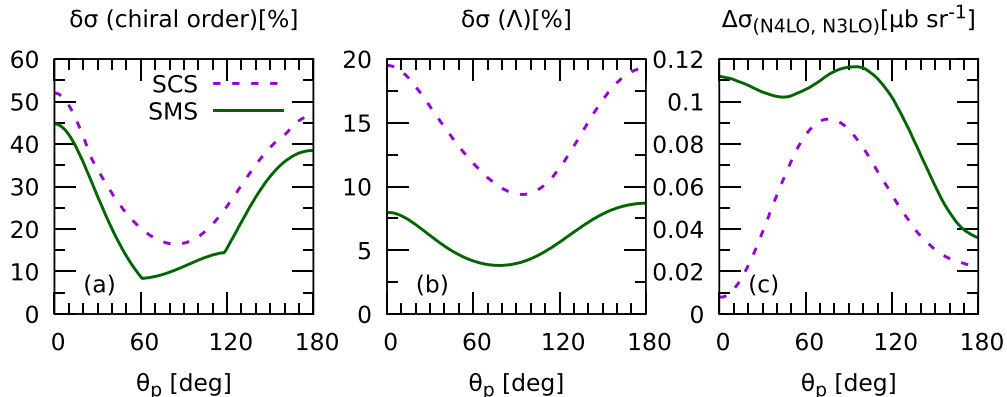


FIG. 5. Same as in Fig. 4 but for  $E_\gamma = 100$  MeV.

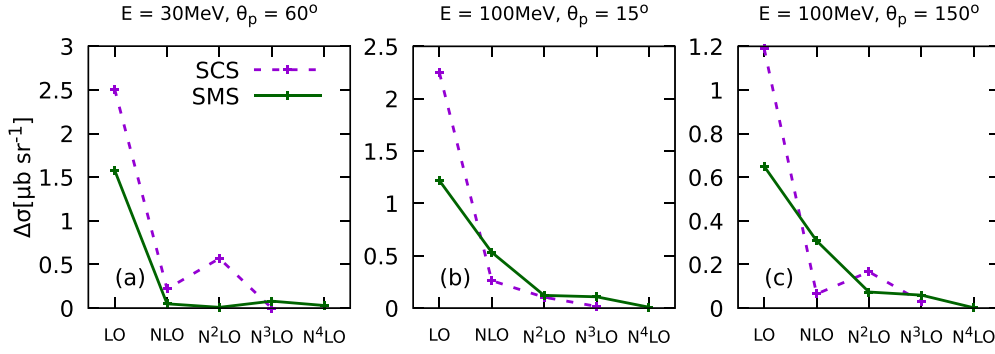


FIG. 6. The absolute difference between the values of the differential cross section  $\frac{d^2\sigma}{d\Omega}$  taken at each of two subsequent chiral orders (the one marked on the  $x$  axis and the next one) at fixed proton angle  $\theta_p$  and photon energy: (a)  $\theta_p = 60^\circ$ ,  $E_\gamma = 30$  MeV, (b)  $\theta_p = 15^\circ$ ,  $E_\gamma = 100$  MeV, and (c)  $\theta_p = 150^\circ$ ,  $E_\gamma = 100$  MeV. The violet dashed (the green solid) line represents results obtained using the SCS (SMS) potential with the cutoff parameter  $R = 0.9$  fm ( $\Lambda = 450$  MeV).

agreement with the results shown in Fig. 4(c). Nevertheless the presence of an additional term  $N^4\text{LO}^+$  in the SMS potential makes the SMS predictions converge as well, though with more terms included. The SMS potential does not reveal a jump between  $N^2\text{LO}$  and  $N^3\text{LO}$  predictions as observed for the SCS force, which is caused by different off-shell behavior of the potential. The more gentle convergence of the SMS potentials can be probably attributed to the removal of the redundant contact interactions, making them much softer than the SCS potentials. Again, as in the case of the comparison with data, it would be interesting to see the convergence pattern of the predictions obtained for both potentials with complete currents.

In Figs. 7 and 8 we give examples of the SMS chiral force predictions for the polarization observables in the deuteron photodisintegration process [39]. Figure 7 presents the photon analyzing power  $A_X$  as a function of the outgoing proton angle  $\theta_p$  at the photon laboratory energy  $E_\gamma = 100$  MeV.

Figure 7(a) shows the dependence of our predictions on the order of the chiral expansion with a fixed regulator  $\Lambda = 450$  MeV. One can see that the few lowest orders of the chiral expansion are not sufficient to obtain convergence, which is achieved only at  $N^3\text{LO}$ . In Fig. 7(b) each curve corresponds to the particular value of  $\Lambda$  (taken as 400, 450, 500, and 550 MeV) used in  $N^4\text{LO}$  calculations. It is clearly visible that for  $A_X$  the dependence on the regulator value is much stronger than for the maximum of the differential cross section (Fig. 1) and amounts to 14%, so in this case a proper choice of the value of the regularization parameter  $\Lambda$  can be important in order to obtain realistic predictions. The comparison between predictions based on the SCS and SMS forces is shown in Fig. 7(c). Clearly, the two forces lead to different values of  $A_X$ , which do not agree even when the truncation errors are taken into account. The SMS potential leads to truncation errors slightly smaller than the ones arising from the SCS force. In Fig. 8 we present the outgoing proton polarization  $P_y$  for

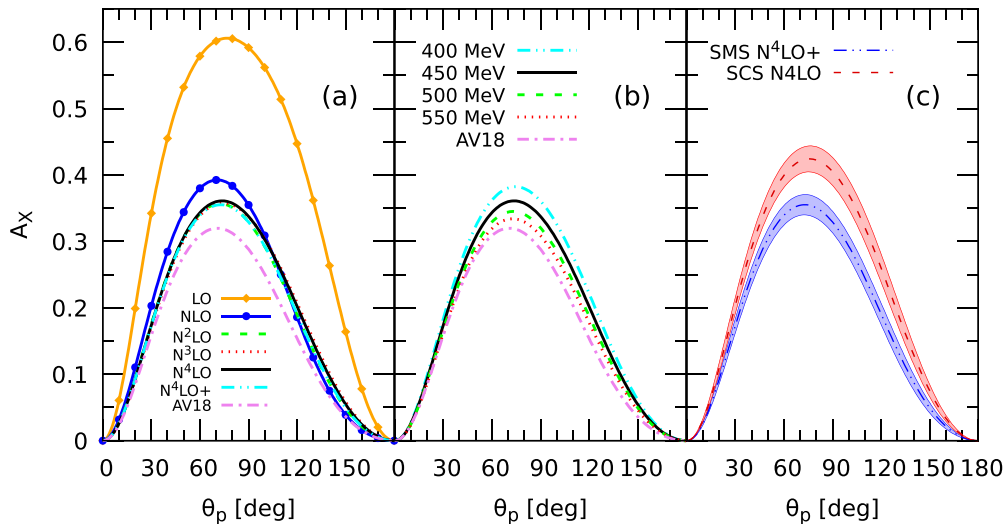
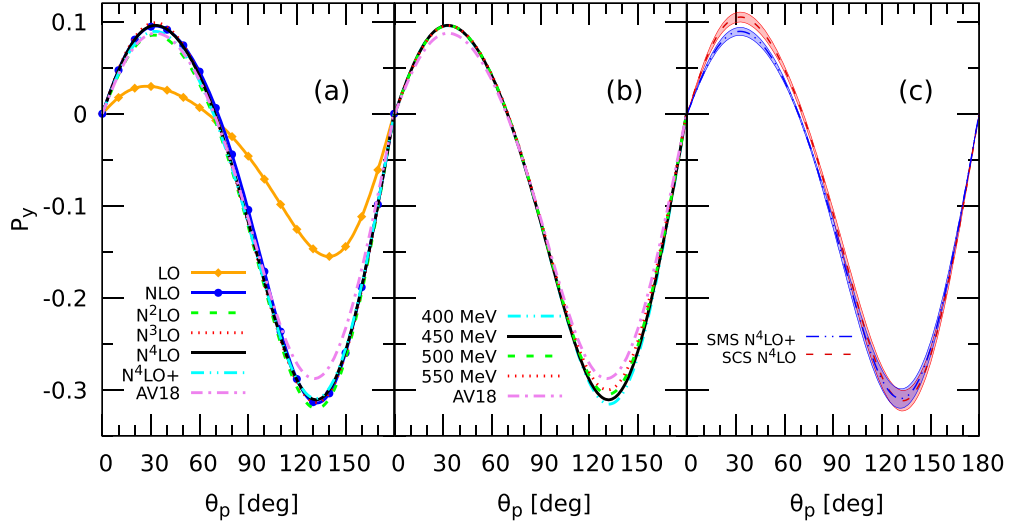


FIG. 7. The photon analyzing power  $A_X$  as a function of the center-of-mass proton detection angle  $\theta_p$  for the deuteron photodisintegration process at  $E_\gamma = 100$  MeV. (a) Dependence of  $A_X$  on the chiral order of the SMS potential at  $\Lambda = 450$  MeV. (b) Dependence of  $A_X$  on the value of the regularization parameter  $\Lambda$  at  $N^4\text{LO}$ . (c) Predictions of the SCS and SMS forces together with truncation errors. Lines in panel (a) are as in Fig. 1(a), those in panel (b) are as in Fig. 1(c), and those in panel (c) are as in Fig. 3(b).

FIG. 8. Same as in Fig. 7 but for the proton polarization  $P_y$ .

the same reaction. The dependence of the predictions on the value of the regulator  $\Lambda$  is slightly weaker for  $P_y$  than for  $A_X$ , since at the minimal values of these observables the relative difference between predictions with different regulator values is less than 5% for  $P_y$  (at  $\theta_p = 131^\circ$ ) and reaches nearly 14% for  $A_X$  (at  $\theta_p = 72^\circ$ ). Also in this case the truncation errors shown in Fig. 8(c) are slightly smaller for the SMS interaction. The SMS and SCS results overlap within uncertainties for the scattering angles above  $90^\circ$  but differ at maximum of the  $P_y$  around  $\theta_p = 35^\circ$ . All our predictions for the deuteron photodisintegration are in a good agreement with the results obtained using the AV18 force and the observed differences

amount to approximately 12% (7%) for  $A_X$  ( $P_y$ ) at their minima.

Now we turn to the neutrino and antineutrino induced deuteron disintegration processes. For obvious reasons we restrict ourselves to the total cross sections  $\sigma_{\text{tot}}$ . These results are obtained from the nuclear response functions generated on dense rectilinear grids of the  $(E_{2N}, Q)$  points, where  $E_{2N}$  is the internal 2N energy and  $Q$  is the magnitude of the three-momentum transfer [32]. Figure 9 presents our predictions for the total cross section  $\sigma_{\text{tot}}$  for the  $\nu_e + {}^2\text{H} \rightarrow \nu_e + p + n$  reaction driven by the neutral current. Again, in Fig. 9(a) we show results obtained using different orders of the chiral expansion (from LO up to  $N^4\text{LO}^+$ ,  $\Lambda = 450$  MeV) and in Fig. 9(b) the variation of the results with respect to the regularization parameter value is presented. For the sake of comparison with the results based on a semiphenomenological potential we also give predictions based on the AV18 interaction. The same dependencies but for the antineutrino induced NC disintegration  $\bar{\nu}_e + {}^2\text{H} \rightarrow \bar{\nu}_e + p + n$  are presented in Fig. 10. The results for the charged-current induced process  $\bar{\nu}_e + {}^2\text{H} \rightarrow e^+ + n + n$  are demonstrated in Fig. 11.

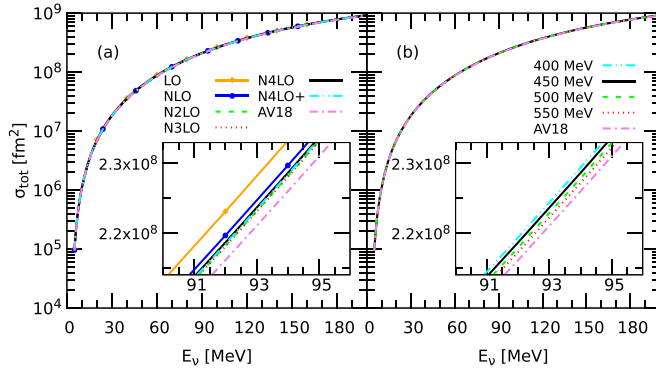


FIG. 9. The total cross section  $\sigma_{\text{tot}}$  for the  $\nu_e + {}^2\text{H} \rightarrow \nu_e + p + n$  reaction as a function of the incoming neutrino energy in the laboratory system. (a) Dependence of  $\sigma_{\text{tot}}$  on the chiral order at  $\Lambda = 450$  MeV. (b) Dependence of  $\sigma_{\text{tot}}$  on the regulator parameter value at  $N^4\text{LO}$ . In panel (a) the orange solid line with diamonds, the blue solid line with circles, and the green dashed, red dotted, black solid, cyan double-dot-dashed, and violet dot-dashed curves correspond to the LO, NLO,  $N^2\text{LO}$ ,  $N^3\text{LO}$ ,  $N^4\text{LO}$ ,  $N^4\text{LO}^+$ , and AV18 potential based predictions, respectively. In panel (b) the cyan double-dot-dashed, black solid, green dashed, red dotted, and violet dot-dashed curves represent results with  $\Lambda = 400, 450, 500$ , and  $550$  MeV and the AV18 based predictions, respectively.

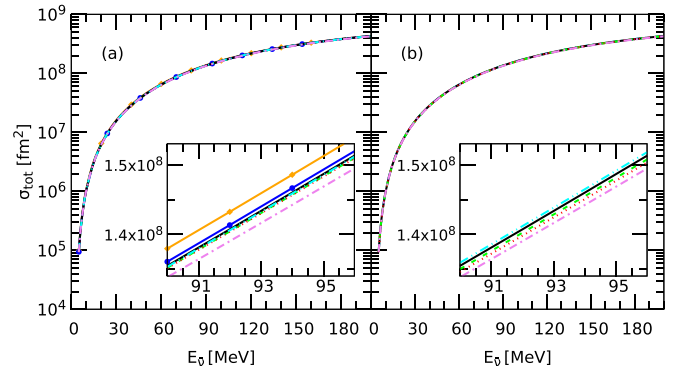


FIG. 10. Same as in Fig. 9 but for the  $\bar{\nu}_e + {}^2\text{H} \rightarrow \bar{\nu}_e + p + n$  reaction.

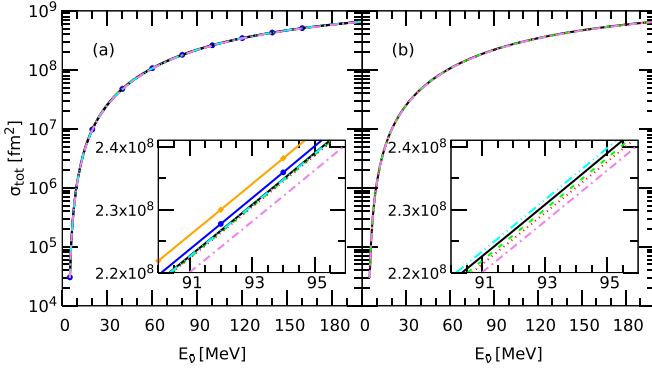


FIG. 11. Same as in Fig. 9 but for the  $\bar{\nu}_e + {}^2\text{H} \rightarrow e^+ + n + n$  reaction.

Because the cross section  $\sigma_{\text{tot}}$  changes by several orders of magnitude over the wide energy range  $E_\nu$ , it is hard to see the differences between curves in Figs. 9–11 with the naked eye. However, in the insets one can see that in Figs. 9(a), 10(a), and 11(a) the two curves, representing the LO and the AV18 predictions, are separated from all the others. It is interesting that the relative position of the different curves in the inset in Fig. 11(a) does not remain the same through the entire energy range. It is the same ordering from zero up to about  $E_\nu = 145$  MeV, but then the LO curve crosses the NLO curve, which has the largest predicted cross section at the higher energies.

In Figs. 9(b), 10(b), and 11(b) are the results of our calculations at  $N^4\text{LO}$  using different regulator values. To give some numerical examples, for the initial particle energy  $E_\nu(\bar{\nu}) = 100$  MeV the relative differences between values

of total cross section  $\sigma_{\text{tot}}$  calculated with the chiral SMS force up to the fifth order ( $N^4\text{LO}$ ) and up to fifth order plus corrections from the sixth order ( $N^4\text{LO}^+$ ) are 0.093% for  $\nu_e + {}^2\text{H} \rightarrow \nu_e + p + n$ , 0.092% for  $\bar{\nu}_e + {}^2\text{H} \rightarrow \bar{\nu}_e + p + n$ , and 0.029% for  $\bar{\nu}_e + {}^2\text{H} \rightarrow e^+ + n + n$  reactions. The relative differences for the cross section obtained using different values of the regularization parameter at the same energy, at  $N^4\text{LO}$ , are 0.96%, 0.98%, and 0.90% for the same reactions, respectively. It is seen that the cutoff dependence is nearly one order bigger than the difference between the last two chiral orders. Nevertheless both uncertainties remain very small, which reflects low sensitivity of these inclusive observables to the employed dynamics. The relative difference of our  $N^4\text{LO}$  and  $N^4\text{LO}^+$  predictions for the last reaction is approximately three times smaller than for the first two reactions. Our treatment of all of the above-mentioned weak reactions is very similar. The common ingredients are the deuteron wave functions and the kinematics, which is only slightly modified due to the small but nonzero positron mass. The single-nucleon weak neutral and charged currents are potential independent so they cannot explain the difference in  $N^4\text{LO}$ – $N^4\text{LO}^+$  spreads for the NC and CC driven reactions. However, the final states for the reactions are different. While in the first two reactions driven by the neutral current a neutron-proton pair emerges in the final state, in the third process,  $\bar{\nu}_e + {}^2\text{H} \rightarrow e^+ + n + n$ , a two-neutron final state is present. Thus the observed variation in spreads stems from the difference between the neutron-neutron and neutron-proton potentials. From Figs. 9–11 it is visible that the AV18 curve deviates somewhat from all the other predictions. However, the difference between the predictions is small and acceptable as the potentials are constructed in quite different ways.

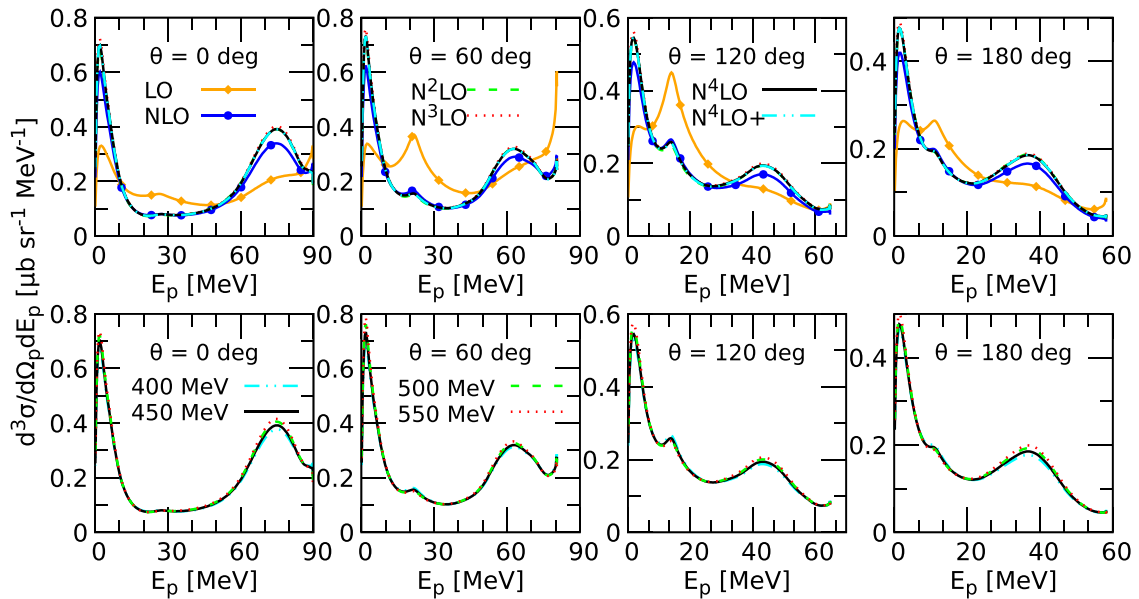


FIG. 12. The semi-inclusive differential cross section  $\frac{d^3\sigma}{d\Omega_p dE_p}$  for the  $\gamma + {}^3\text{He} \rightarrow p + p + n$  reaction at  $E_\gamma = 120$  MeV as a function of the outgoing proton energy  $E_p$  at different values of the polar angle of the outgoing proton momentum  $\theta_p$ . Top row: Cross-section dependence on the order of chiral expansion (at  $\Lambda = 450$  MeV). Bottom row: Dependence on the value of the regularization parameter  $\Lambda$ . The curves are as in Fig. 1 but the AV18 prediction is not shown here.



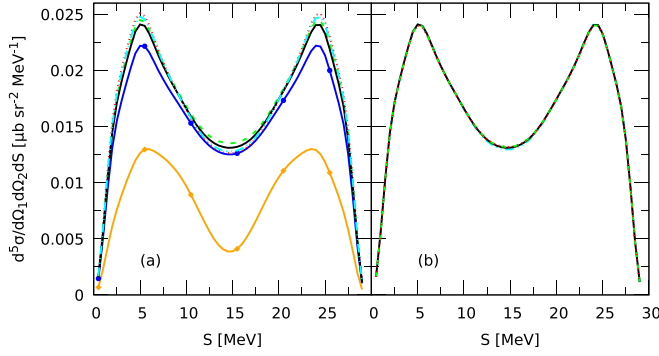


FIG. 13. The fivefold differential cross sections  $\frac{d^5\sigma}{d\Omega_1 d\Omega_2 dS}$  for the complete kinematical configuration with the two protons detected at  $\Theta_1 = 15^\circ$ ,  $\Phi_1 = 0^\circ$ ,  $\Theta_2 = 15^\circ$ , and  $\Phi_2 = 180^\circ$  angles for the  $^3\text{He}$  photodisintegration process at the photon energy  $E_\gamma = 40$  MeV in the laboratory frame. (a) Dependence on the chiral order (with  $\Lambda = 450$  MeV). (b) Results for different regulator values (at  $N^4\text{LO}$ ). Curves are as in Fig. 12.

#### IV. $^3\text{He}$ PHOTODISINTEGRATION

In this section we discuss our calculations for the  $^3\text{He}$  photodisintegration process  $\gamma + ^3\text{He} \rightarrow p + p + n$  using the SMS chiral potentials. As in the  $^2\text{H}$  case we use the Siegert theorem to go beyond the SNC approximation [28]. In the following we neglect the three-nucleon interaction. The semi-inclusive differential cross section  $\frac{d^3\sigma}{d\Omega_p dE_p}$  for the photon laboratory energy  $E_\gamma = 120$  MeV is presented in Fig. 12. Each of the four columns corresponds to a particular angle of the outgoing proton momentum with respect to the photon beam in the laboratory system ( $0^\circ$ ,  $60^\circ$ ,  $120^\circ$ , and  $180^\circ$ , respectively). The top row shows the dependence of our predictions on the order of the chiral expansion. As in Figs. 1, 7, and 8 we see that it is not enough to take into account only leading and next-to-leading orders to achieve convergence of the predictions and one has to include higher orders of the chiral expansion. It is interesting to note that the older SCS potential seems to converge even faster as the NLO line in Fig. 12 is farther from the higher-order curves than the corresponding one in Fig. 9 of [17], where the predictions of the SCS chiral force for the same observable are shown. This is similar to the already observed picture for the deuteron photodisintegration.

The bottom row represents the regulator dependence of the cross section, which proves to be weak. For most of the proton energies the maximum difference between all predictions remains below 10%. There are only exceptions for the outgoing proton angle  $0^\circ$  and its energies greater than 80 MeV, where the difference amounts to 20%, and for the angle  $180^\circ$  at proton energies around 40 MeV, where it reaches 12%. The regulator dependence revealed by the SMS chiral force is weaker than is observed for the SCS force (compare Fig. 11 in Ref. [17]).

The fivefold differential cross section  $\frac{d^5\sigma}{d\Omega_1 d\Omega_2 dS}$  for the same process is presented in Fig. 13 for the photon laboratory energy  $E_\gamma = 40$  MeV for two protons detected at the following polar and azimuthal angles (assuming that the momentum

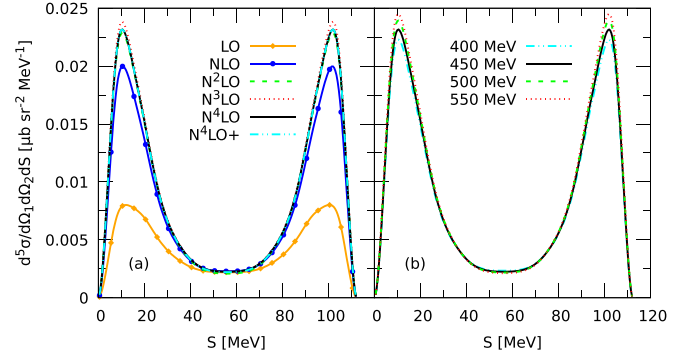


FIG. 14. Same as in Fig. 13 but for  $E_\gamma = 120$  MeV.

of the initial photon  $\vec{p}_\gamma$  is parallel to the  $z$  axis):  $\Theta_1 = 15^\circ$ ,  $\Phi_1 = 0^\circ$  and  $\Theta_2 = 15^\circ$ ,  $\Phi_2 = 180^\circ$ . The arc length  $S$  of the kinematical locus in the  $E_1$ - $E_2$  plane, where  $E_1$  and  $E_2$  are the kinetic energies of the two detected nucleons, is used to uniquely define the kinematics of the three-body breakup reaction [47]. We observe that the NLO contribution is very important since it raises the LO cross section by a factor of 2. An additional shift (around 9%) comes from  $N^2\text{LO}$  and only small changes are seen when  $N^3\text{LO}$ ,  $N^4\text{LO}$ , and  $N^4\text{LO}^+$  force components are included. However, even for the highest orders ( $N^4\text{LO}$  and  $N^4\text{LO}^+$ ) curves do not overlap, which suggests that full convergence is not achieved yet. With respect to the regulator dependence the picture is more stable, since it is very hard to distinguish individual predictions in Fig. 13(b).

Figure 14 shows the cross section for the same choice of polar and azimuthal angles as presented in Fig. 13 but for the higher incoming photon energy  $E_\gamma = 120$  MeV. The general trends do not change with increasing energy, except for the fact that the dependence on the regularization parameter is slightly stronger, which is visible at the maxima of the cross sections around  $S = 15$  and 100 MeV. But for all other values of the arc-length parameter  $S$  almost full agreement between all the lines exists.

#### V. SUMMARY AND CONCLUSIONS

We presented the results of the application of the chiral NN potential with the semilocal regularization in momentum space to a number of electroweak reactions: the  $^2\text{H}$  and  $^3\text{He}$  photodisintegrations and the (anti)neutrino induced deuteron breakup reactions:  $\gamma + ^2\text{H} \rightarrow p + n$ ,  $\gamma + ^3\text{He} \rightarrow p + p + n$ ,  $\nu_e + ^2\text{H} \rightarrow \nu_e + p + n$ ,  $\bar{\nu}_e + ^2\text{H} \rightarrow \bar{\nu}_e + p + n$ , and  $\bar{\nu}_e + ^2\text{H} \rightarrow e^+ + n + n$ . In the case of the  $^3\text{He}$  photodisintegration we focus on the properties of the applied NN potential and neglect the three-body force.

All our results show a weaker, compared to the previous version of the Bochum-Bonn chiral potential (the SCS force), dependence on the regularization parameter  $\Lambda$ . A small spread of results obtained with different values of  $\Lambda$  make the predictions based on the current interaction model less ambiguous. We also observe good convergence of the predictions with respect to the chiral order and the possibility to include some terms from the sixth order ( $N^4\text{LO}^+$ ) favorably distinguishes the SMS force from the SCS one.

As we have no full 2N electromagnetic current consistent with the SMS interaction at our disposal, the Siegert theorem was used to take two-nucleon contributions in the electromagnetic current operator at least partly into account for the photodisintegration processes. As a consequence, the incomplete electromagnetic current operator leads to some problems with the data description, as seen in Fig. 1. We expect that future application of the electromagnetic current operator fully consistent with the 2N potential will significantly improve the agreement with the data.

The presented polarization observables for the deuteron photodisintegration processes ( $A_X$  and  $P_y$ ) are the observables for which the slowest convergence with respect to the chiral order and the strongest dependence on the regularization parameter are noticed. For instance, for the deuteron analyzing powers ( $T_{11}$ ,  $T_{20}$ ,  $T_{21}$ , and  $T_{22}$ ) the convergence is very fast (above the leading order) and the regulator variation is negligible.

The same picture is also valid for the investigated total cross sections for the weak  $^2\text{H}$  disintegrations via neutral or charged currents: the convergence with respect to the chiral order is quite rapid and the regulator dependence is weak.

The new SMS potential has a number of practical advantages in comparison to the previous SCS potential. Its predictions show weaker dependence on the regularization parameter and good convergence with respect to the order of the chiral NN potential. There is still room for improvement in our calculations. The main drawback of the present formalism is the lack of the explicit electroweak current operator

entirely consistent with the 2N SMS interaction as well as the omission of the three-nucleon force for the  $^3\text{He}$  disintegration. To achieve that ambitious goal requires in the first step a construction of consistent and reliable two- and three-nucleon forces. Investigations along this line are conducted using the SMS regularization scheme within the LENPIC project. After establishing the interactions, consistently regularized currents, fulfilling the continuity equation, will be applied to electroweak processes. In addition, future complete studies should be supplemented with an analysis of truncation errors using the Bayesian approach, which would allow one to draw more reliable conclusions about the convergence pattern of chiral EFT predictions for these reactions. Nevertheless, our results with the simplified Hamiltonian reveal the usefulness of the SMS chiral force for studies of various electroweak processes in few-nucleon systems in the near future.

### ACKNOWLEDGMENTS

This work is a part of the LENPIC project and was supported by the Polish National Science Center under Grants No. 2016/22/M/ST2/00173 and No. 2016/21/D/ST2/01120. It was also supported in part by BMBF (Grant No. 05P18PCFP1) and by Deutsche Forschungsgemeinschaft through funds provided to the Sino-German CRC 110 project “Symmetries and the Emergence of Structure in QCD” (Grant No. TRR110). The numerical calculations were partially performed on the supercomputer cluster of the JSC, Jülich, Germany.

- 
- [1] P. Reinert, H. Krebs, and E. Epelbaum, *Eur. Phys. J. A* **54**, 86 (2018).
  - [2] E. Epelbaum, H.-W. Hammer, and Ulf-G. Meißner, *Rev. Mod. Phys.* **81**, 1773 (2009).
  - [3] R. Machleidt and D. R. Entem, *Phys. Rept.* **503**, 1 (2011).
  - [4] M. Piarulli, L. Girlanda, L. E. Marcucci, S. Pastore, R. Schiavilla, and M. Viviani, *Phys. Rev. C* **87**, 014006 (2013).
  - [5] E. Epelbaum, H. Krebs, and U.-G. Meißner, *Phys. Rev. Lett.* **115**, 122301 (2015).
  - [6] V. Bernard, E. Epelbaum, H. Krebs, and Ulf-G. Meißner, *Phys. Rev. C* **77**, 064004 (2008).
  - [7] V. Bernard, E. Epelbaum, H. Krebs, and Ulf-G. Meißner, *Phys. Rev. C* **84**, 054001 (2011).
  - [8] D. R. Entem, R. Machleidt, and Y. Nosyk, *Phys. Rev. C* **96**, 024004 (2017).
  - [9] A. Ekström, G. Baardsen, C. Forssen, G. Hagen, M. Hjorth-Jensen, G. R. Jansen, R. Machleidt, W. Nazarewicz, T. Papenbrock, J. Sarich, and S. M. Wild, *Phys. Rev. Lett.* **110**, 192502 (2013).
  - [10] A. Gezerlis, I. Tews, E. Epelbaum, S. Gandolfi, K. Hebeler, A. Nogga, and A. Schwenk, *Phys. Rev. Lett.* **111**, 032501 (2013).
  - [11] E. Epelbaum, H. Krebs, and U.-G. Meißner, *Eur. Phys. J. A* **51**, 53 (2015).
  - [12] E. Epelbaum, J. Golak, K. Hebeler, H. Kamada, H. Krebs, U.-G. Meißner, A. Nogga, P. Reinert, R. Skibiński, K. Topolnicki, Yu. Volkotrub, and H. Witała, *Eur. Phys. J. A* **56**, 92 (2020).
  - [13] Yu. Volkotrub, J. Golak, R. Skibiński, K. Topolnicki, H. Witała, E. Epelbaum, H. Krebs, and P. Reinert, *J. Phys. G* **47**, 104001 (2020).
  - [14] R. Skibiński, J. Golak, H. Witała, W. Glöckle, A. Nogga, and E. Epelbaum, *Acta Phys. Pol. B* **37**, 2905 (2006).
  - [15] R. Skibiński, J. Golak, D. Rozpędzik, K. Topolnicki, and H. Witała, *Acta Phys. Pol. B* **46**, 159 (2015).
  - [16] D. Rozpędzik, J. Golak, S. Kölling, E. Epelbaum, R. Skibiński, H. Witała, and H. Krebs, *Phys. Rev. C* **83**, 064004 (2011).
  - [17] R. Skibiński, J. Golak, K. Topolnicki, H. Witała, E. Epelbaum, H. Krebs, H. Kamada, Ulf-G. Meißner, and A. Nogga, *Phys. Rev. C* **93**, 064002 (2016).
  - [18] R. B. Wiringa, V. G. J. Stoks, and R. Schiavilla, *Phys. Rev. C* **51**, 38 (1995).
  - [19] E. Epelbaum, H. Krebs, and P. Reinert, *Front. Phys.* **8**, 98 (2020).
  - [20] D. Riska and G. Brown, *Phys. Lett. B* **38**, 193 (1972).
  - [21] D. O. Riska, *Phys. Scr.* **31**, 107 (1985); **31**, 471 (1985).
  - [22] J. Carlson and R. Schiavilla, *Rev. Mod. Phys.* **70**, 743 (1998).
  - [23] H. Arenhövel and M. Schwamb, *Eur. Phys. J. A* **12**, 207 (2001).
  - [24] L. E. Marcucci, M. Viviani, R. Schiavilla, A. Kievsky, and S. Rosati, *Phys. Rev. C* **72**, 014001 (2005).
  - [25] S. Kölling, E. Epelbaum, H. Krebs, and U.-G. Meißner, *Phys. Rev. C* **84**, 054008 (2011).
  - [26] A. Baroni and R. Schiavilla, *Phys. Rev. C* **96**, 014002 (2017).
  - [27] A. A. Filin, V. Baru, E. Epelbaum, H. Krebs, D. Möller, and P. Reinert, *Phys. Rev. Lett.* **124**, 082501 (2020).

- [28] J. Golak, R. Skibiński, H. Witała, W. Glöckle, A. Nogga, and H. Kamada, *Phys. Rept.* **415**, 89 (2005).
- [29] J. Golak, R. Skibiński, H. Witała, K. Topolnicki, A. E. Elmeshneb, H. Kamada, A. Nogga, and L. E. Marcucci, *Phys. Rev. C* **90**, 024001 (2014).
- [30] J. Golak, H. Kamada, H. Witała, W. Glöckle, J. Kuroś, R. Skibiński, V. V. Kotlyar, K. Sagara, and H. Akiyoshi, *Phys. Rev. C* **62**, 054005 (2000).
- [31] J. Golak, R. Skibiński, K. Topolnicki, H. Witała, A. Grassi, H. Kamada, and L. E. Marcucci, *Phys. Rev. C* **98**, 015501 (2018).
- [32] J. Golak, R. Skibiński, K. Topolnicki, H. Witała, A. Grassi, H. Kamada, and L. E. Marcucci, *Phys. Rev. C* **100**, 064003 (2019).
- [33] H. Krebs, PoS **CD2018**, 098 (2020).
- [34] S. Kölling, E. Epelbaum, H. Krebs, and U.-G. Meißner, *Phys. Rev. C* **80**, 045502 (2009).
- [35] H. Krebs, E. Epelbaum, and U.-G. Meißner, *Ann. Phys. (NY)* **378**, 317 (2017).
- [36] H. Krebs, E. Epelbaum, and U.-G. Meißner, *Few Body Syst.* **60**, 31 (2019).
- [37] H. Krebs, E. Epelbaum, and Ulf-G. Meißner, *Eur. Phys. J. A* **56**, 240 (2020).
- [38] Low Energy Nuclear Physics International Collaboration, [www.lenpic.org](http://www.lenpic.org)
- [39] H. Arenhövel and M. Sanzone, *Few Body Syst. Suppl.* **3**, 1 (1991).
- [40] S. Binder *et al.* (LENPIC Collaboration), *Phys. Rev. C* **93**, 044002 (2016).
- [41] R. J. Furnstahl, N. Klco, D. R. Phillips, and S. Wesolowski, *Phys. Rev. C* **92**, 024005 (2015).
- [42] S. Q. Ying, E. M. Henley, and G. A. Miller, *Phys. Rev. C* **38**, 1584 (1988), and references therein.
- [43] E. De Sanctis *et al.*, *Phys. Rev. Lett.* **54**, 1639 (1985).
- [44] M. Hoferichter, J. Ruiz de Elvira, B. Kubis, and U.-G. Meißner, *Phys. Rev. Lett.* **115**, 192301 (2015).
- [45] V. G. J. Stoks, R. A. M. Klomp, M. C. M. Rentmeester, and J. J. de Swart, *Phys. Rev. C* **48**, 792 (1993).
- [46] S. Binder, A. Calci, E. Epelbaum, R. J. Furnstahl, J. Golak, K. Hebeler, T. Hüther, H. Kamada, H. Krebs, P. Maris, Ulf-G. Meißner, A. Nogga, R. Roth, R. Skibiński, K. Topolnicki, J. P. Vary, K. Vobig, and H. Witała (LENPIC Collaboration), *Phys. Rev. C* **98**, 014002 (2018).
- [47] W. Glöckle, H. Witała, D. Hüber, H. Kamada, and J. Golak, *Phys. Rept.* **274**, 107 (1996).